316L Stainless-Steel Carburizing Close to Eutectic Transformation Using the Spark Plasma Sintering Process

Yoann Pinot, Aurélien Besnard, Maria-Rosa Ardigo-Besnard, and Florian Bussière

This work focuses on the 316L austenitic stainless-steel case-hardening microstructure, after the SPS process near the solid/liquid state transition temperature. This process, faster than conventional carburizing techniques, is equivalent to weld cladding, allowing the achievement of high surface carbon contents with large-size carbide grains in the case of partial melting. Three distinct zones were formed: internal carburizing, carburizing with melting, and carburizing with melting and chromium depletion; all three composed of mixed carbides $(Cr_{0.4}Fe_{0.6})_7C_3$ distributed in an austenitic matrix. The internal carburizing layer growths following a parabolic kinetic law with $k_p^{(i)} \approx 10^{-7}$ cm^2/s, while the advancement of the melting front is very fast and follows a linear law with $k_l = 1.0 \times 10^{-4}$ cm^2/s at 1100 °C. The Cr-depleted fusion zone microstructure is similar to a composite material with a metallic matrix, which includes graphite particles, Mo-rich intermetallic phases, and core-shell eutectic carbides. The partial melting zone without Cr depletion shows the formation of a dense carbide layer with diameters exceeding 10 μm, constituting 60% of the volume, and achieving a hardness of 850 HV_5. Its wear rate is about 100 times lower than the 316L steel, indicating a significant improvement in the alloy's wear behavior.

Keywords 316L powder, carburizing, core-shell chromium carbide, eutectic transformation, spark plasma sintering (SPS), wear behavior

1. Introduction

The spark plasma sintering (SPS) process is a technology that combines the application of uniaxial pressure and pulsed direct current, enabling simultaneous powder consolidation and heating via the Joule effect. During the SPS process, the powder is wrapped in graphite sheets to ensure good electrical, physical, and thermal contact with the graphite tooling (die and punches). However, the main disadvantage of the SPS process is the carbon contamination of the sintered materials from the tooling or/and graphite foils whether for alloys (Ref 1) or ceramics (Ref 2). Necina and Pabst (Ref 3) reduced the thermal gradients and carbon contamination on transparent spinels by driving the current with a sawtooth signal. Other works focused on the use of a barrier layer to limit carbon diffusion with carburigenic elements such as Mo, Ta (Ref 4), and Ti (Ref 5). In contrast, Nishimoto and Nishi (Ref 6) took advantage of this phenomenon to carry out a case-hardening treatment to modify the mechanical surface characteristics of the titanium alloys and improve their wear resistance. Alternatively, carbon for case-hardening in the SPS process can be supplied through methods such as blending graphite powder with metal powder (Ref 7) or incorporating carbon fibers (Ref 8). The advantage of using a sheet of graphite to enrich the material with carbon makes the process easier avoiding an additional carbon source.

Another feature of the SPS process is local melting and/or evaporation between the powder particles (Ref 9), or even the complete sample melting by runaway Joule heating (Ref 10). Therefore, it is possible to modify the material surface composition and microstructure by adding carbon and by melting the surface, without altering the bulk, like weld cladding techniques (Ref 11). Thus, the novelty of this study lies in employing the SPS process as a surface treatment technique, inducing local melting to create eutectic carbides (Ref 12), with the primary goal of enhancing the mechanical properties, particularly the wear resistance, of austenitic stainless steels. The present study focuses on the 316L austenitic stainless-steel microstructure after case-hardening by the SPS process near the solid/liquid state transition temperature. The growth kinetics of chromium carbides are discussed. The wear behavior was also assessed as a function of the carbides' morphology and their volume fraction in the material.

2. Materials and Method

The AISI 316L austenitic stainless-steel powder (Aubert&-Duval) presents a particle size ranging from 63 to 90 μm. The samples were sintered using an SPS HPD 10 apparatus. A

Yoann Pinot and **Aurélien Besnard**, Arts et Metiers Institute of Technology, LaBoMaP, Université Bourgogne Franche-Comté, HESAM Université, 71250 Cluny, France; **Maria-Rosa Ardigo-Besnard** and **Florian Bussière**, Laboratoire Interdisciplinaire Carnot de Bourgogne (ICB), UMR 6303 CNRS, Université de Bourgogne, BP 47870, 21078 Dijon, Cedex, France. Contact e-mail: yoann.pinot@ensam.eu.

cylindrical graphite mold of 30 mm inner diameter, 90 mm outer diameter, and 50 mm height (Fig. 1a) was filled with 28 g of powder to obtain a solid disc of 30 mm in diameter and 5 mm in height. Graphite foils (0.35 mm thick) previously inserted between the powder and the mold, cover all the inner surfaces of the mold and, therefore, are in contact with all sample surfaces (Fig. 1, faces A and B). Sintering was carried out at 1100 °C for seven different durations (from 5 to 40 min) under vacuum (10^{-2} mbar) and a pressure of 70 MPa. The heating and cooling rates were 50 °C min^{-1} and more than 100 °C min^{-1}, respectively. In the present study, local melting microstructure analyses and wear tests were focused on two samples (25 and 30 min with partial melting), while the other samples were used for the determination of carbides growth kinetics and carbon diffusion study.

After sintering, the specimens were cut, embedded in resin, and polished with SiC papers (up to 1200 grit) and diamond paste (from 9 to 1 μm). Microstructural studies were carried out using optical microscope (OM) and scanning electron microscope (FEG-SEM). The SEM is coupled to an energy-dispersive x-ray spectrometer for elemental analysis, performed at 15 keV. Elemental quantification of case-hardening areas located at different depths from the surface was also carried out by spark spectroscopy after successive polishing steps. Crystallographic phase identification was performed by x-ray diffraction in θ-2θ Bragg-Brentano configuration, using Cu Kα = 1.5418 Å. Microhardness profiles were performed on samples cross sections with a Vickers indenter and a load of 100 gf. Macrohardness measurements were carried out on the samples surfaces with a Vickers indenter and a load of 5 kgf.

Wear resistance was evaluated with a pin-on-disk configuration. WC/Co ball of 6 mm in diameter was used as a counterface to slide against polished (P800) samples without lubrication. Wear tests were undertaken under different normal loads, covering te full available range: 1, 5, and 10 N. For all loads, the test was set at 4000 cycles, with a constant linear speed of 5 cm/s, corresponding to the optimum condition allowing the steady state to be observed in an acceptable time. The mean tangential forces are plotted as a function of the three normal loads (1, 5, and 10 N), which plot a line, according to Coulomb's friction law. The friction coefficient, independent from the load, is then statistically determined from the slope coefficient. The depth of the wear tracks depth was estimated using an optical profilometer.

3. Results and Discussion

3.1 Microstructure

Figure 1 shows OM views of the cross-section of the sample sintered at 1100 °C for 25 min under 70 MPa.

Figure 1(b) shows the cross-sectional microstructure of face A (Fig. 1a), the top sample surface. The chromium carbide formation attains a depth of about 690 μm from the surface; a denser carbide layer of approximately 340 μm from the surface is observable. This dense layer is due to the surface melting, where chromium carbides correspond to the dark gray areas. In the internal carburizing zone under the dense carbide layer, the carbides are firstly located in the grains, to finally localize at the grain boundaries far from the surface. When the powder has high electrical conductivity, the DC pulse passes through the compacted powder, generating spark plasma, spark impact pressure (Ref 9), Joule heating (Ref 13), and electric field (Ref 9). The spark discharge in the narrow spaces between the powder particles induces a locally high-temperature state. Moreover, in conductive powders, temperature at the necks formed between particles can rise rapidly to the alloy melting point (Ref 14). In addition, Joule effect runaway (Ref 10) can occur by the liquid phase formation. Figure 1(c) presents the cross-sectional microstructure of face B (Fig. 1a), the lateral sample surface. The carburizing depth is about 400 μm, without abnormal carbides size, i.e., without melting. This carburizing difference between faces A and B results from the uniaxial application of the pressure and the current (forced diffusion), as well as from the presence of a thermal gradient at

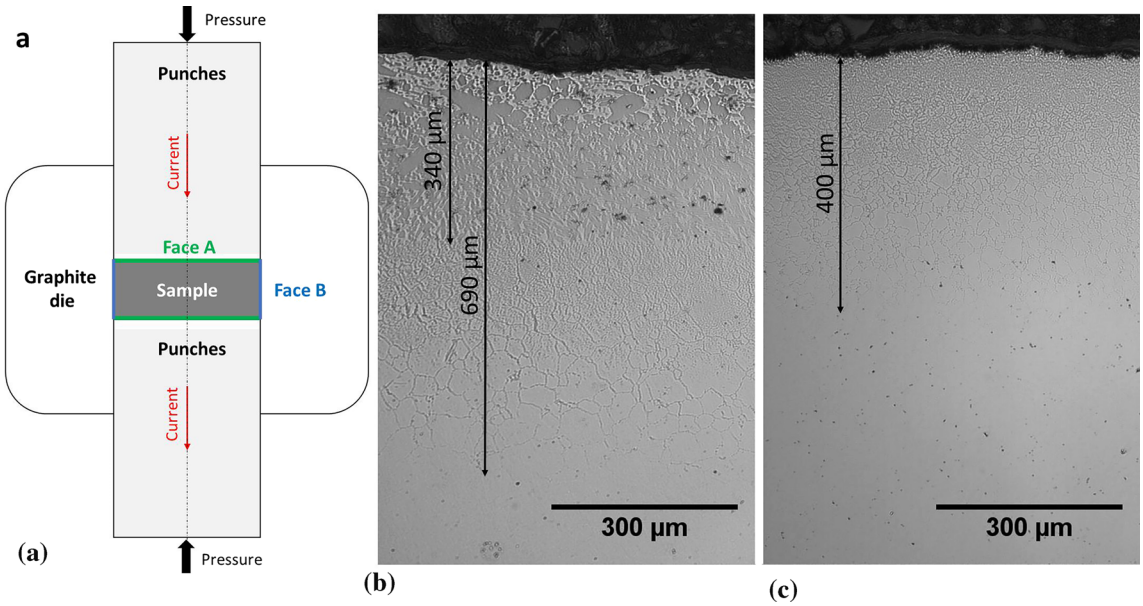

Fig. 1 (a) Schematic cross-sectional representation of the SPS device. Optical microscope views of the sample sintered at 1100 °C under 70 MPa for 25 min: (b) side perpendicular to the current and the pressure (face A) and (c) side parallel to the current and the pressure (face B)

the tool/sample interface. The current distribution in the die and the powder affects the heat distribution and the mass transport phenomena. It depends on the tooling geometry and the electrical conductivity of the sintered material. In the case of a non-conductive sample, the current preferentially passes through the die, which heats the sample by thermal conduction and radiation. In the case of a conductive sample, the current passes through the sample and the graphite die. Anselmi-Tamburini et al. (Ref 13) observed a higher current density on the sample surfaces than in the bulk for conductive copper samples. Moreover, the current density distribution is heterogeneous between the sample surfaces: the surface perpendicular to the current direction (Face A in the present study) shows a higher current density than the surfaces parallel to the current direction (Face B in the present work). A higher temperature is also observed at the center of the sample than at its edge. In addition, the pressure applied by the punches during sintering is probably heterogeneously distributed over the sample. The pressure enhances the sample densification and limits the grain size; however, for short times or low temperatures, it is common to observe a higher porosity at the edge of the sample than in the bulk (Ref 15).

XRD analysis of the sample surface perpendicular to the current (Face A) (Fig. 2) confirms the presence of $(Cr, Fe)_7C_3$, austenite, and graphite. Phases were indexed from ICDD data available in the database of EVA software: (04-017-0806), (00-056-0159), and (04-009-1699), respectively.

The austenitic phase with a face-centered cubic structure (fcc) corresponds to the 316L alloy matrix. The presence of only one graphite peak indicates strong texturing of the hexagonal hcp structure along the (004) direction. It is attributed to the remaining graphite foil fragments on the sample surface. The mixed (Fe, Cr) carbides show several peaks, similar to a powder diffractogram, without any preferential orientation. The patterns of the carbide phase fit well with $(Cr_{0.5}Fe_{0.5})_7C_3$ stoichiometry, having an orthorhombic structure and the following lattice parameters: a = 4.52 Å, b = 6.97 Å, and c = 12.07 Å. EDS analyses will allow to refine the determination of the stoichiometry.

Table 1 presents EDS analyses, after carbon deconvolution, performed in several zones inside the sintered samples. Indeed, carbon quantification via the EDS technique is difficult, mainly due to surface contamination (e.g., from carbon resin), and

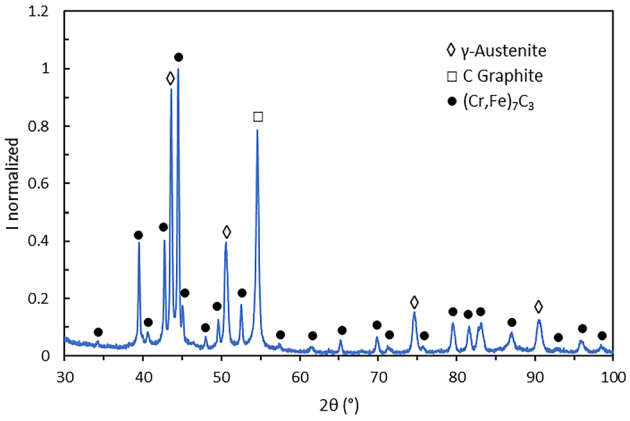

Fig. 2 XRD patterns of the surface perpendicular to the current (Face A) of the sample sintered at 1100 °C under 70 MPa for 25 min

requires special precautions (cold finger and use of a standard sample).

The quantitative analyses of the metallic elements indicate, for carbides, a stoichiometry corresponding to $(Cr_{0.4}Fe_{0.6})_7C_3$, in agreement with the literature (Ref 16, 17). The analyses showed no significant difference in the carbide stoichiometry, whatever the observed zones. The presence of the M_7C_3 carbides is in agreement with the 316L equilibrium phase diagram (Fig. 3), calculated for a powder composition (in wt.%) of 17.7 Cr, 0.83 Si, 1.88 Mn, 2.44 Mo, 11.9 Ni.

At 1400 K (about 1100 °C), for carbon contents lower than 1 wt.% (4.5 at.%), $M_{23}C_6$ cohabits mainly with the austenitic phase. For carbon contents between 1 and approximately 1.5 wt.% (6.6 at.%), a zone of $M_{23}C_6$ and M_7C_3 cohabitation is observed in the austenitic phase. Above 1.5 wt.% C, M_7C_3 are exclusively observed in the austenitic phase, reaching carbon saturation in the alloy and graphite formation for carbon contents above 5.5 wt.% (21.3 at.%) at 1400 K. The increase in carbon content leads to a decrease in the solid/liquid transition temperature. Thus, for carbon contents higher than 5.5 wt.% (21.3 at.%), the solid/liquid transition is close to 1435 K. According to the thermodynamic diagram, $M_{23}C_6$ carbides should be found in the sintered samples, but they were not detected by XRD analyses.

Figure 4 shows the evolution of the average carbides diameter, their quantity as well as the associated sample hardness as a function of the case hardening depth and the zone impacted by melting.

The carbide diameter was determined by the equivalent mean circle diameter method (ISO 13383) and the volume fractions by image processing (thresholding and counting pixels with ImageJ). Two main carburized zones are present: a melted zone at the surface of the sample and an internal carburizing one. In the internal carburizing zone, the average diameter of the carbides is about 3 μm (Fig. 4, Green curve). The carbides are initially located at the grain boundaries due to intergranular carbon diffusion. The carbide formation inside the grains (intragranular diffusion) is also observed for higher carbon contents towards the surface (Fig. 4, SEM image). During the melting of the sample surface, the size of the carbides strongly increases. The first carbides, formed by internal carburizing due to carbon diffusion from the graphite foil during the heating step of the SPS process, serve as a seed for the growth of large carbides in the melt. Indeed, the M_7C_3 carbides have a higher melting temperature than the matrix and remain solid while the austenitic matrix melts. The carbon supply to the carbides is no longer limiting, due to high solubility and fast diffusion of carbon in the liquid alloy. The SEM image at the bottom of Figure 4 shows that, in the melting zone, the carbides have elongated hexagonal morphology, typical of hexagonal crystallographic structure (Ref 18, 19). The formation of carbides is the result of the decrease in the solubility of carbon between liquid and solid. The carbon content regulates the amount of formed carbides and determines the type of carbides and their morphology (Ref 12). The surface fraction of carbides (Fig. 4, Blue curve) increases towards the surface. A maximum of 60% is observed in the middle of the melting zone (≈ 150 μm depth), while the fraction decreases to 40% in the near-surface (≈ 30 μm depth).

Figure 5 shows the depth composition profile made by spark spectroscopy for a sample sintered at 1100 °C under 70 MPa for 30 min.

Table 1 EDS analyses at 15 keV with carbon deconvolution of different zones inside the sintered samples at 1100 °C under 70 MPa for 25 and 30 min

Composition, at.%	Fe	Cr	Ni	Mo	Mn	Si	O
Reference alloy	64.1 ± 0.2	19.6 ± 0.2	11.2 ± 0.3	1.5 ± 0.1	1.9 ± 0.1	1.7 ± 0.2	
Carbides	55.5 ± 5.3	38.0 ± 5.4	2.3 ± 0.3	2.3 ± 0.5	1.9 ± 0.1	0.0 ± 0.0	
Alloy in melting and carburizing zones	70.0 ± 2.4	4.6 ± 1.0	20.0 ± 2 .7	0.5 ± 0.1	1.7 ± 0.1	3.2 ± 0.5	
Intermetallic in the melting zone	20.7 ± 3.9	9.2 ± 0.8	1.8 ± 0.5	65.7 ± 3.9	2.2 ± 0.2	0.4 ± 0.1	
Oxide in wear track	27.2 ± 4.7	8.7 ± 4.4	4.3 ± 0.7	0.7 ± 0.1	0.8 ± 0.1	0.9 ± 0.2	57.4 ± 8.4

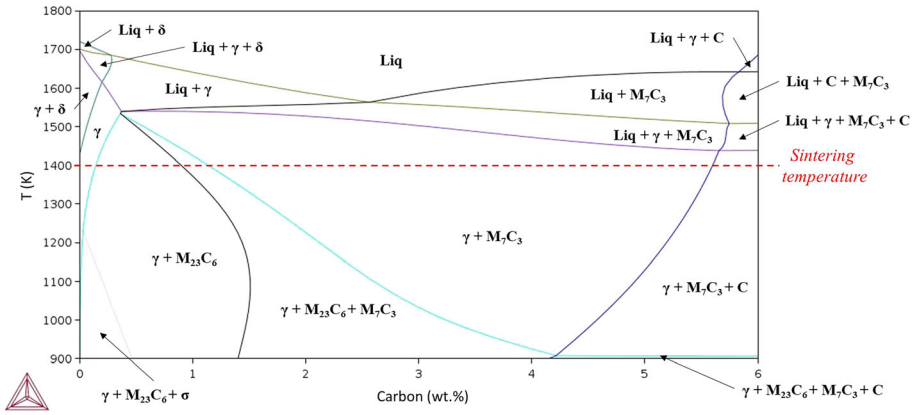

Fig. 3 316L equilibrium diagram calculated from Thermo-Calc with the TCFE12 database (version 2022a. https://thermocalc.com/products/databases/steel-and-fe-alloys/)

The surface microstructure is similar for samples sintered at 25 and 30 min, with the presence of the two zones: the melting zone and the internal carburizing one. Consistently with the hardness evolution reported in Figure 4, two zones are also observed in the melting area: one corresponding to a Cr-depleted zone near the surface from 0 to 0.06 mm depth, and the second one corresponding to a carbide-rich zone from 0.06 to 0.8 mm depth. Chromium was mainly consumed in the front of the melting, corresponding to the carbide-rich zone with 60% of carbides (Fig. 4). The matrix elements (Fe and Ni) tend to decrease from the Cr-depleted zone to the carbide-rich zone. Internal carburizing in the solid state is found beyond a depth of 0.8 mm. The evolution of the carbon content follows Fick's law in the form of an exponential function. The carbon content at the partial melt to solid state transition is about 5 wt.%. There is also a slight depletion of chromium in this area with a content of 15 wt.%. For the sake of clarity, the minor alloying elements (Mo, Si, and Mn) are not presented in Figure 5. However, the EDS data show a constant Mo content with penetration depth. For Mn and Si, a slightly lower content is observed in the melting zone compared to the bulk. These elements have a high affinity with the matrix, e.g., Mn stabilizes the austenitic phase (Ref 20). The evolution of the macro-hardness follows the same trend as the amount of carbide in the alloy (Fig. 4). A hardness of $\approx$ 550 HV_5 is measured at the near-surface in the Cr-depleted zone and reaches a maximum of $\approx$ 850 HV_5 in the carbide-rich zone in the melting zone. The thickness of this carbide-rich zone is about 160 μm. The inner carbide zone near the melt/solid transition shows a hardness of 500 HV_5 ($\approx$ 270 μm deep), while the bulk hardness is about 180 HV_5. Local indentations at a very low load of 25 gf on the near-surface made it possible to determine the hardness of the Cr_7C_3 carbide, i.e., 1619 $HV_{0.025}$ ± 36 in agreement with the literature (Ref 21, 22). The matrix hardness in the melted zone is 313 $HV_{0.025}$ ± 15.

Figure 6 shows the EDS mapping performed on the three areas of interest after carburization.

Figure 6(a) corresponds to the near-surface of the sample, which has undergone partial melting with Cr depletion and formation of abnormal size carbides ($\approx$ 5.7 wt.% C). Figure 6(b) shows the carbide-rich zone with partial melting and no Cr depletion ($\approx$ 9.8 wt.% C). Finally, Figure 6(c) shows the internal carbide zone near the partial melting zone ($\approx$ 3.2 wt.% C). A difference in microstructure between the three zones can be observed, both in terms of morphology and amount of carbides. Whatever the zone, Fe, Ni, and Si are preferentially located in the austenitic phase (Table 1). The measured values in the austenitic phase are slightly higher than those measured in the bulk. Carbides are mainly formed by chromium and iron. However, the iron content in the carbide is significantly lower than the one measured in the bulk and in the austenitic matrix in the melting zone. The Mo mapping indicates segregation in the melted zone. Increasing Mo and Ni contents tend to decrease the solubility of carbon in steel (Ref 20). EDS analyses (Table 1) revealed the presence of a Mo-rich intermetallic phase containing also Fe and Cr, not identified by XRD, because of its low quantity and small crystallite size. According to the literature (Ref 23), an intermetallic μ phase (hexagonal R3 $\bar{m}$ Frank-Kasper phase family) and Mo-rich areas for Fe-Mo compounds elaborated by SPS were observed. An intermetallic phase, $Fe_{0.35}Mo_{0.65}$, in the austenitic matrix, in addition to core-shell carbides $(Cr, Fe)_7C_3$, and $(Cr, Fe)_{23}C_6$ were observed in composites (316L/carbide) obtained by LMD process (Ref 12).

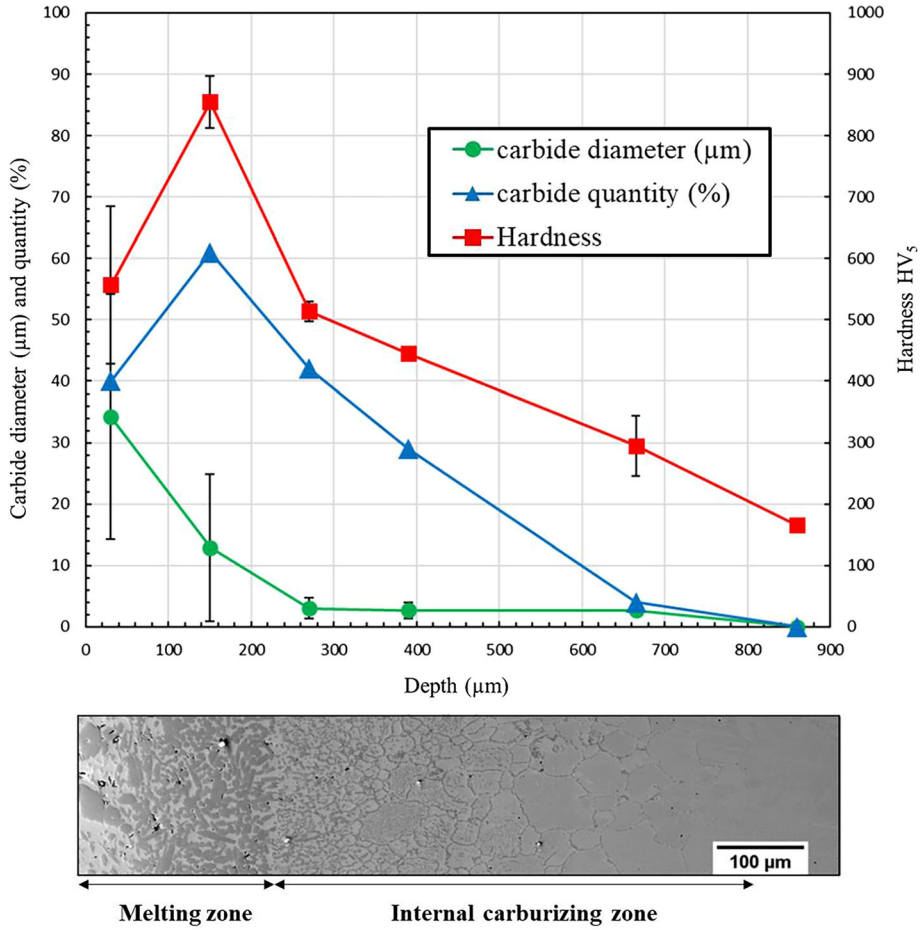

Fig. 4 Evolution of hardness, size, and carbides' amount and a SEM image (cross section) as a function of depth for a sample sintered at 1100 °C under 70 MPa for 25 min

Figure 7(a) shows a SEM cross-sectional image of the Cr-depleted melted zone.

The presence of black areas is attributed to graphite fragments from the foil, the light grey area corresponds to the austenitic matrix, and the dark grey areas correspond to chromium carbides. The Cr-depleted melting zone is therefore similar to a composite material (graphite + Cr_7C_3 in a metal matrix) (Ref 12). The observation of graphite in the sample is in agreement with the phase equilibrium diagram (Fig. 3), indicating that carbides and graphite exist at carbon contents above 4.2 wt.% at 900 K. A magnification (Fig. 7b) shows that the carbide has a core-shell morphology with a central reservoir of iron and nickel trapped during the coalescence and growth of carbides in the melt. In as-cast and as-welded 316L steel the Cr-rich M_7C_3 primary carbide is the first phase to form during cooling below the liquidus temperature before the austenite solidification. When the liquid has been consumed, the final product is composed of (γ + M_xC_y). The stoichiometry of the primary carbides will depend on chromium, iron, and carbon contents in the alloy. When the possibility of solid-state diffusion is limited due to the rapid cooling rate, the $M_7C_3 \rightarrow M_{23}C_6$ transformation may not occur or may stop at a transient stage to form a core-shell structure. The transition can occur either from the center of the primary Cr_7C_3 carbide (Ref 24) or from its periphery (Ref 25), depending on the formation conditions. Traces of M_3C are also observed in the case of fast solidification during rapid cooling (Ref 25, 26).

3.2 Growth Kinetics of Carbides

During sintering, the carbon from the graphite foil dissolves in the alloy and diffuses inward to react with the chromium of the matrix, leading to the precipitation of carbides. The chromium carbides formation results from the competition between two processes: the formation of a continuous surface layer results from the rapid diffusion of chromium toward the surface, whereas internal carburizing results from the rapid diffusion of carbon into the material ($D_C > > D_{Cr}$). Figure 8 shows the evolution of the depth of carbide formation in the sintered samples for different holding times. The green curve represents the samples sintered with an average power of around 420 W, delivered during the temperature rise. The SPS process is controlled according to ramps (heating and cooling) and the holding temperature. Consequently, it will deliver the requested power to reach the temperature setpoint, according to the feedback measured by the pyrometer. Therefore, the power is not driven but endured. These samples did not undergo partial melting, only internal carburizing. The precipitation depth X(i) (Ref 27) increases according to parabolic growth kinetics: $X^2_{(i)} = 2k_p^{(i)}t$. $k_p^{(i)}$ is the parabolic internal carburizing constant. This indicates that the process is diffusion driven. k_p is related to the carbon permeability D_cN_c in the alloy, according to the approximations of the Wagner equation (Ref 27): $k_p^{(i)} = \frac{D_cN_C^{(s)}}{\nu N_{Cr}^{(0)}}$. $N_c^{(s)}$ is the surface solubility of carbon in the

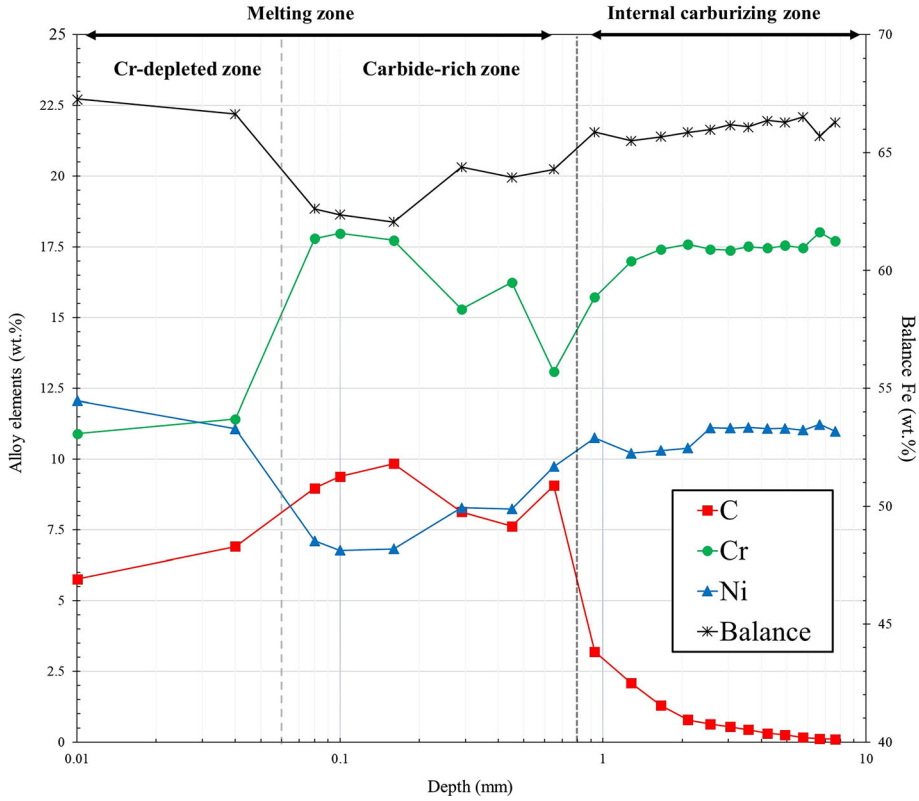

Fig. 5 Spark spectroscopy analyses of carburizing depth composition evolution for a sample sintered at 1100 °C under 70 MPa for 30 min

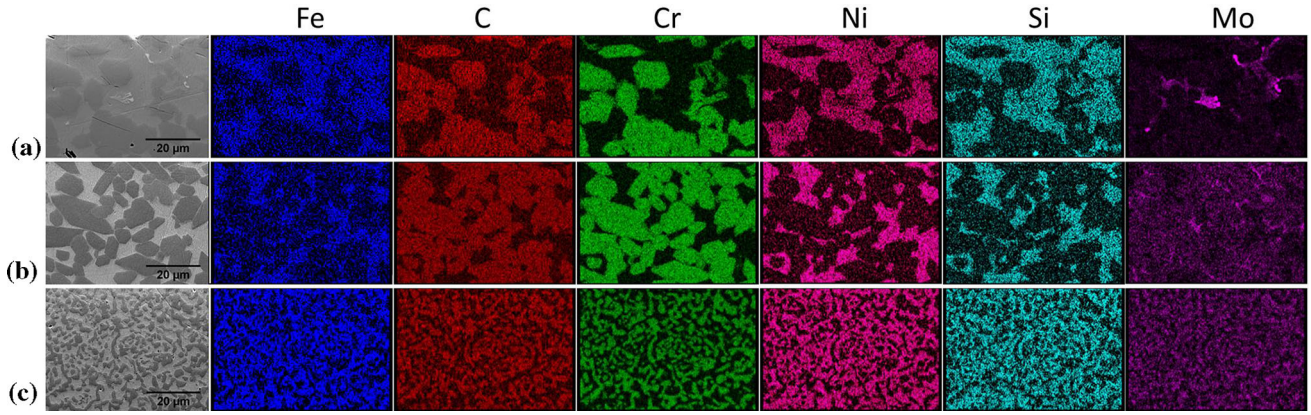

Fig. 6 EDS mapping on plane vue for a sample sintered at 1100 °C under 70 MPa for 30 min: (a) melting zone with Cr depletion; (b) melting zone without Cr depletion; (c) internal carburizing without melting

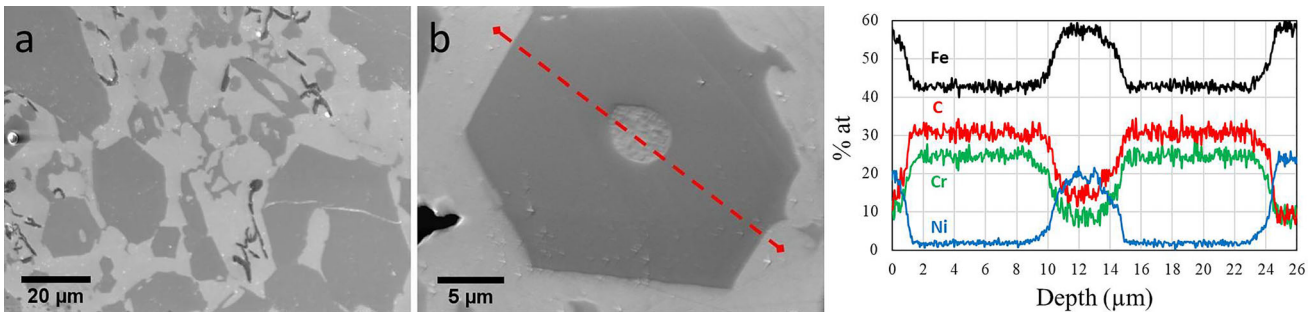

Fig. 7 SEM analyses in the melting zone with Cr depletion for a sample sintered at 1100 °C under 70 MPa for 30 min: (a) SE image of carbides and lamellar graphite morphologies; (b) SE zoomed-in image of a core-shell carbide with the corresponding EDS profile

steel at 1100 °C, $N_{Cr}^{(0)} \approx 0.2$ is the initial chromium concentration in the alloy, D_c is the diffusion coefficient of carbon in the steel, and v is the stoichiometric constant of the carbide, represented in the equation: $Cr + vC = CrC_v$. In the case of the mixed carbide $(Cr_{0.4}Fe_{0.6})_7C_3$, the stoichiometric constant is $v = 1.07$ and tends to decrease with the chromium content to reach $v = 0.42$ for the Cr_7C_3 stoichiometry. The transformation of M_7C_3 carbides into $M_{23}C_6$ during annealing shows a decrease in the iron stoichiometry of the M_7C_3 carbide due to the more favorable thermodynamic conditions. Thus, v will tend to decrease for the best thermodynamic stability. From the 316L equilibrium diagram (Fig. 3), the solubility of carbon at the steel surface is estimated to be $N_c^{(s)} \approx 0.06$ at 1100 °C. Face B (Fig. 1c) has also been studied. Although the points are not shown on the graph, the internal carburizing also follows a parabolic law. Table 2 presents the carbon diffusion coefficients and internal carburizing constants calculated from micrographic and microhardness analyses of 316L steel at 1100 °C according to the sample faces (Fig. 1) exposed during the SPS process.

The diffusion coefficient calculated from the actual carbides' stoichiometry shows a slight increase compared to Cr_7C_3 carbides. The difference in internal carburizing kinetics between faces A and B results from a temperature gradient caused by the current distribution between the faces of the sample. These results are in agreement with the observations in Fig. 1.

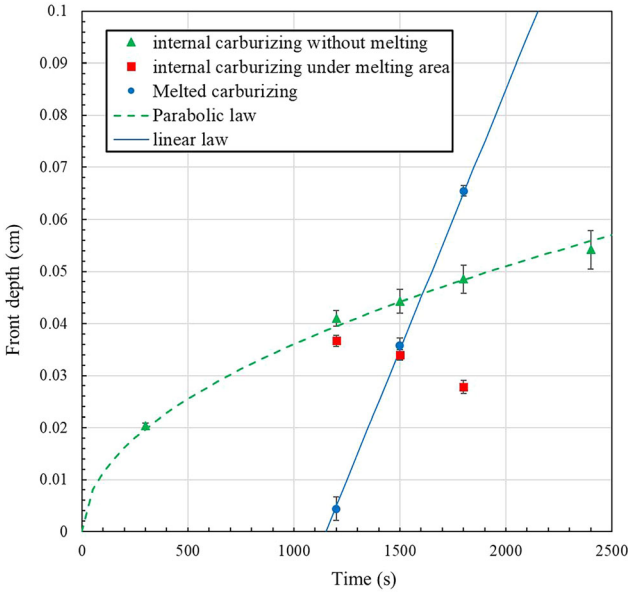

Fig. 8 Carburizing depth as a function of sintering time

Figure 8 shows the kinetic growth of carburizing for samples sintered without melting (Fig. 8, green curve) and with melting (Fig. 8 blue curve) at 1100 °C under 70 MPa for holding times from 5 to 40 min. The red squares (Fig. 8) represent the depths impacted by internal carburizing under the melting area. The samples with melting zone were sintered with an average power of 440 W during the temperature rise. The temperatures measured with the pyrometer are identical for all the samples presented in this study (1100 °C). However, it is not uncommon to observe SPS hot spots on the sample surface, undetectable by the pyrometer. The difference in the average delivered power between the two batches can be explained by a different electrical contact between the powder and the tooling, which favors the formation of melting points via the Joule effect runaway. The diffusion of carbon in the sample also favors the lowering of the transition temperature (Fig. 3). The spark spectroscopy analyses carried out on the surface of the sample treated for 40 min at 1100 °C without melting give a carbon content close to 4.5 wt.%. As the temperature rises, a significant amount of carbon diffuses into the alloy. However, melting does not occur directly, it is necessary to have a holding time of at least 20 min with an average temperature rise power of approximately 440 W to reach a critical carbon content. The depth of advance of the melting front $X_{(m)}$, increases according to linear growth kinetics: $X_{(m)} = k_l^{(m)} t$. The advance constant of the melting front is $k_l = 1.0 \times 10^{-4}$ cm²/s. The carbon supply to the carbides is no longer a limiting phenomenon for carbide growth, due to rapid diffusion and high solubility of C in the liquid phase compared to the solid state. Carbon diffusion in the alloy follows parabolic kinetics when there is no partial melting. Due to the presence of the graphite sheet, it is assumed that the carbon concentration at the surface is constant and that the diffusion coefficient remains constant over the concentration range studied. Thus, the diffusion profile can be modeled using the solution of Fick's second law (Ref 28) for a semi-infinite sample: $\frac{(C_x - C_0)}{(C_s - C_0)} = 1 - \mathrm{erf}\left[\frac{x}{2\sqrt{Dt}}\right]$. C_0 is the initial carbon concentration in the sample [$C_0 = C(x, t = 0)$], C_s is the carbon concentration at the sample surface [$C_s = C(z = 0, t)$], D is the apparent diffusion coefficient of carbon in the alloy, and erf(x) the error function. One method to determine the carbon concentration profile in steels is through micro-hardness analyses. This can be done by determining graphically the distance at which the hardness of the carbon-enriched zone approaches the bulk hardness. Consequently, the diffusion coefficient of carbon in the steel can be determined from

Table 2 Parabolic kinetic constants, diffusion coefficients, activation energy, and pre-exponential factor calculated from micrographic (Fig. 8) and microhardness (Fig. 9) analyses

	From micrographic analyses		From microhardness analyses		
	k_p, cm²/s	D_C, cm²/s at 1100 °C	D, cm²/s at 1100 °C	Q, kJ/mol	D_0, cm²/s
Face A	6.5×10^{-7}	9.1×10^{-7} for Cr_7C_3 2.3×10^{-6} for $(Cr_{0.4}Fe_{0.6})_7C_3$	4.3×10^{-9}	46.9	2.6×10^{-7}
Face B	4.5×10^{-7}	6.3×10^{-7} for Cr_7C_3 1.6×10^{-6} for $(Cr_{0.4}Fe_{0.6})_7C_3$	3.9×10^{-9}	51.5	3.5×10^{-7}

$\frac{(HV_x - HV_0)}{(HV_s - HV_0)} = 1 - \mathrm{erf}\left[\frac{x}{2\sqrt{Dt}}\right]$. HVs is the sample surface hardness (600 HV) and HV_0 is the initial hardness in the "bulk" steel (200 HV). The Vickers hardness filiations carried out under a load of 100 gf are presented in Figure 9(a) and (b) for samples sintered without melting at 1100 °C.

The evolution of the hardness as a function of the penetration depth fits well the model (dashed curve). The homogeneous distribution of the carbides in the volume and their small sizes as a function of the carburizing depth can explain a hardness evolution similar to the diffusion of C in a solid solution. However, using this approach for the partial melting zone is not appropriate. The hardness filiations allowed to determine the apparent diffusion coefficients for the A side (surfaces perpendicular to the current direction) with $D = 5.0 \times 10^{-7}$ cm^2/s and the B side (parallel to the current direction) with $D = 3.4 \times 10^{-7}$ cm^2/s, respectively. These diffusion coefficients are in agreement with the ones determined from the k_p in Figure 8 (Table 2). The apparent carbon diffusion coefficient includes the contribution of intergranular diffusion, intragranular diffusion, and the number of precipitated carbides. The interstitial diffusion of carbon in steel is thermally activated, so the apparent diffusion coefficient can also be expressed according to Arrhenius law: $D = D_0 \exp^{(\frac{-Q}{RT})}$. D_0 is the pre-exponential factor, and Q is the activation energy of the apparent diffusion of carbon in the steel. Q and D_0 are obtained by plotting ln(D) as a function of $1/T$: the linear regression constant is equal to ln(D_0) and the slope to $-Q/R$ (R is the perfect gas constant $R = 8.314$ J K^{-1} mol^{-1}). The Arrhenius law (Fig. 9c) was plotted from 88 filiations and 33 samples, taking into account the average temperature over the whole thermal cycle. Indeed, the temperature ramps (heating and cooling) during sintering are not neglectable. They are equivalent to an average temperature of 772 °C with a holding time of 1071 s, which allows the diffusion (intergranular or mixed).

Activation energy $Q = 46.9$ kJ/mol and $D_0 = 2.6 \times 10^{-7}$ cm^2/s are calculated for the A side (solid line) and $Q = 51.5$ kJ/mol and $D_0 = 3.5 \times 10^{-7}$ cm^2/s are obtained for the B side (dashed line) (Table 2). Non-exhaustive research data from the literature on the carburizing of austenitic steels show an activation energy range from 156 to 35 kJ/mol, for diffusion coefficients ranging from 1.0×10^{-6} to 3.0×10^{-11} cm^2/s (Ref 29-32). The diffusion mechanism depends on the experimental conditions (case hardening process, atmosphere, ...) and the material metallurgical state (carbide precipitations, carbon in solid solution, ...). The diffusion coefficients and activation energies calculated in this study are in the same order of magnitude as those reported in the literature. The calculated diffusion coefficient associated with the Arrhenius law is $D \approx 10^{-9}$ cm^2/s at 1100 °C. This value is lower than the calculated coefficient $D \approx 10^{-7}$ cm^2/s from the growth constant (Fig. 8). The difference is due to the use of an average time-temperature equivalent to determine the Arrhenius law, in contrast to the use of the holding time at 1100 °C to determine the growth constant. The diffusion coefficient of side A is higher than that of side B for an activation energy $Q_B > Q_A$.

In the case of the Cu/Ti couple (Ref 33), a faster diffusion in SPS than in conventional sintering was observed, with a lower activation energy for the SPS process. Indeed, the plasma and electric field induced by the pulsed DC during the treatment promotes the migration of atoms, ions, and vacancies, which reduce the treatment time. During SPS of a Si/Mo couple (Ref 34), the diffusion was improved by the current. However, no significant difference were found in the activation energy for $MoSi_2$ formation between sintering with and without current. The current does not alter the reaction mechanism and a faster diffusion with current improves defect mobility but also phase nucleation and growth rate.

3.3 Wear Resistance/Wear Behavior

According to Coulomb's law, the dynamic friction force (F_T) is independent of the relative sliding speed of the two surfaces. The coefficient of friction (μ) is proportional to F_T and F_N (force normal to the surface) according to $\mu = \frac{F_T}{F_N}$. The friction coefficient depends principally on the nature of the materials in contact (sample, counterpart, and eventually a third body). The sample surface topographies before the wear tests are all equivalent (polished surface P800), i.e., Ra ≈ 0.02 μm. Table 3 shows the average friction coefficients. Three values are presented: initial state from 0 to 10 cycles, steady state from 3000 to 4000 cycles and the average value from 0 to 4000 cycles.

Whatever the sample, the friction coefficient μ is approximately the same for the first 10 cycles, corresponding to a 10 cm friction distance (μ ranges between 0.1 and 0.14). This low value is attributed to the WC/steel contact. The presence of

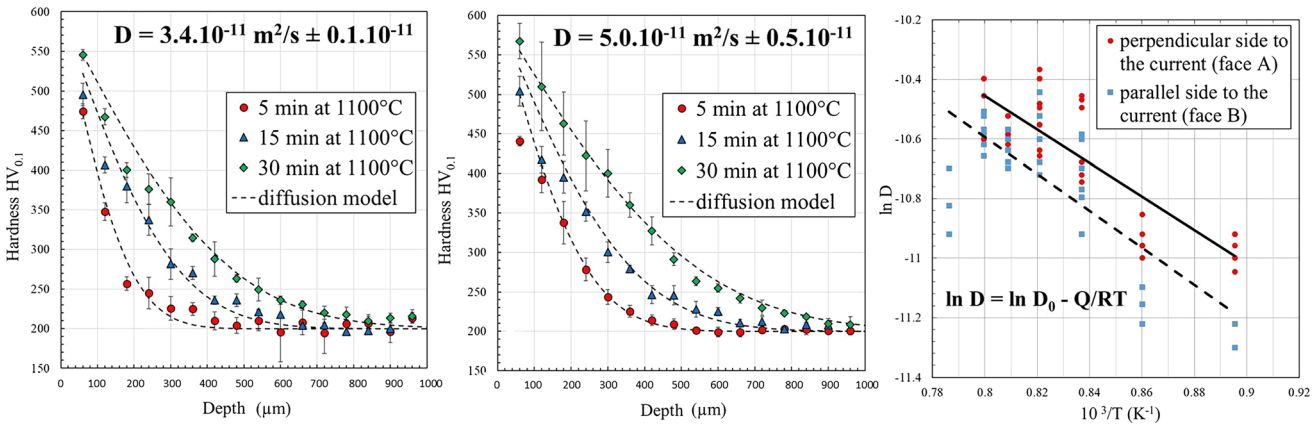

Fig. 9 Vickers hardness $HV_{0.1}$ measurement along the carburizing depth (a) for face B (Fig. 1c), and (b) for face A (Fig. 1c); (c) Arrhenius plots for the rate constant of the internal carburizing of Cr_7C_3 following sample side

Table 3 Friction coefficients determined from the linear slope coefficients of F_T versus F_N for the face A of sample carburized by SPS at 1100 °C under 70 MPa for 30 min

Samples	From 0 to 10 cycles	From 3000 to 4000 cycles	From 0 to 4000 cycles
316L	0.10 ± 0.03	0.52 ± 0.03	0.50 ± 0.04
Internal carburizing	0.12 ± 0.01	0.60 ± 0.08	0.58 ± 0.01
Melting zone without Cr depletion	0.14 ± 0.01	0.56 ± 0.07	0.42 ± 0.08
Melting zone with Cr depletion	0.13 ± 0.01	0.66 ± 0.07	0.54 ± 0.03

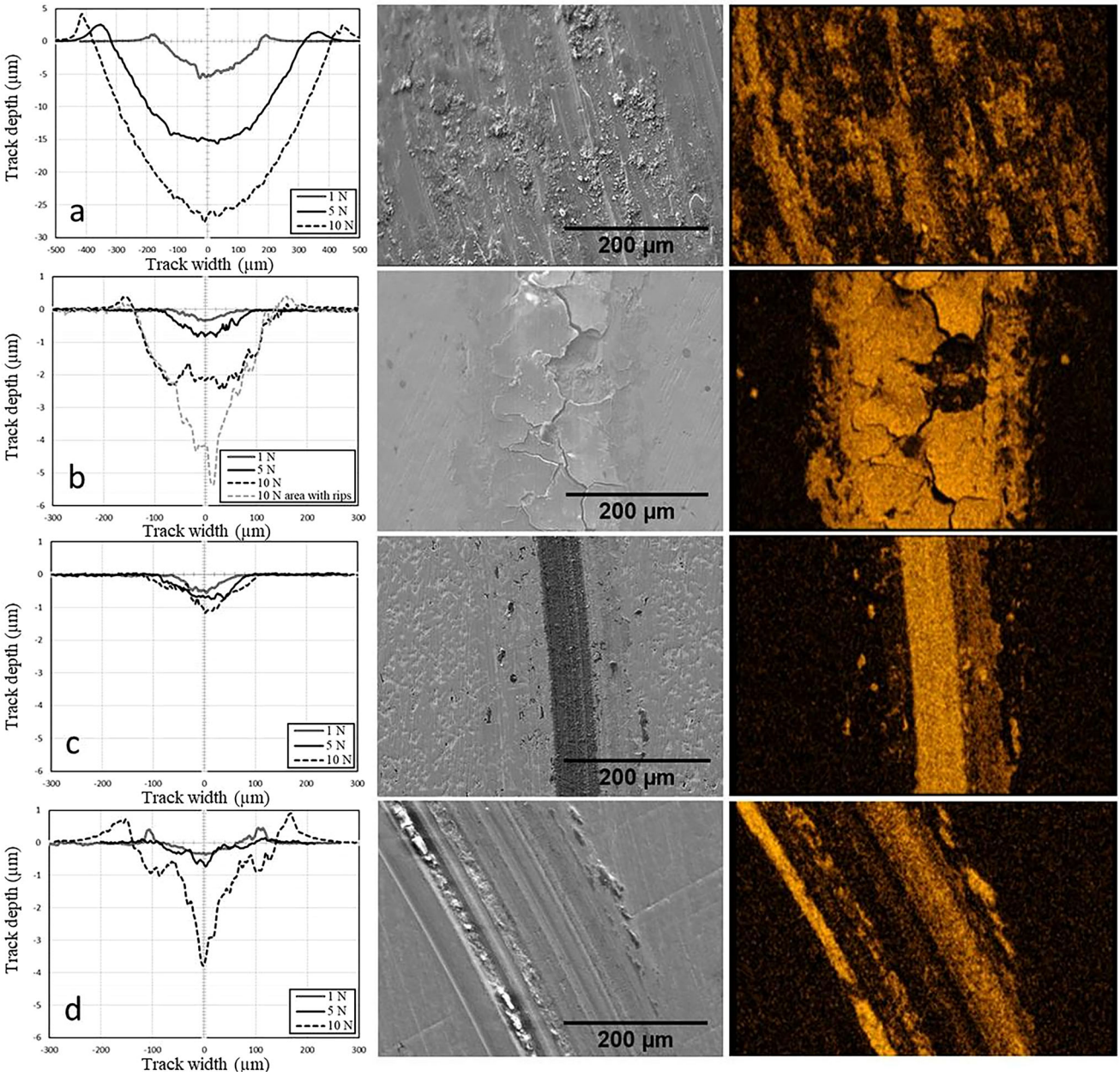

Fig. 10 From left to right: wear track profiles under different loads, SEM image of the wear track under 10 N and its associated oxygen EDS mapping for (a) 316L; (b) Cr depletion melting zone; (c) melting zone without depletion; (d) internal carburizing zone on the face A of the sample carburized by SPS at 1100 °C under 70 MPa for 30 min

chromium carbides on the steel surface tends to slightly increase the μ value. During the first stages, the contact temperature increases excessively, favoring the oxide layer formation on the surface of the sample, for a friction coefficient value between 0.5 and 0.6 in the steady state (Table 3) in agreement with the literature (Ref 35, 36). The overall μ value

of 316L and internal carburizing samples remains close to the steady state value. In means that, μ evolves very quickly from the beginning of the test without a long running-in period. The coefficient of friction for the two melted zones shows an average overall value below the stable value, which corresponds to a slow increase in μ during the test. The difference in average value between these two zones may be due to the difference in size, amount of chromium carbides, and Mo-rich intermetallic phases present on the surface. Figure 10 shows the wear track depth, SEM image, and EDS mapping of oxygen associated to wear tests performed under 10 N.

The EDS mapping indicates the presence of oxide in the wear track for each sample; its stoichiometry (Table 1) suggests hematite $(Fe_{0.8}Cr_{0.2})_2O_3$ phase. The debris pushed to the edge of the wear track has a red color, typical of this type of oxide. SEM image and EDS mapping of the wear track of the bulk 316L sample (Fig. 10a) show the presence of very small oxide debris trapped in the wear track. The depth of wear tracks increases with the increasing applied load. The profiles of the wear tracks are smooth parabolic shapes without deep grooves. SEM image (Fig. 10b) of the carburized sample with partial melting and Cr depletion shows the presence of oxide plates surrounded by cracks. The cracking oxidized zone is the result of thermal and mechanical stress, due to the volume expansion caused by the phase change and a different expansion coefficient between oxide and metal. Oxide plate spalling is also observed. The difference in track depth between the oxidized and spalled areas (Fig. 10b) is of the order of 3 μm, corresponding to the thickness of the oxidized layer. It appears that oxidation is very significant in this sample, due to chromium depletion. Oxidative wear is the predominant mechanism. Any effect of the presence of Mo-rich precipitates and graphite on the wear behavior of the melt-impacted zones was observed. Wear track of carburized sample with partial melting without Cr depletion (Fig. 10c) shows an oxide layer formed on the surface, which remains well adherent to the steel surface, unlike the oxide layer of the other tested samples. SEM image and EDS mapping of the wear track of the carburized sample without partial melting (Fig. 10d) show the presence of debris trapped in the wear track and leading to the abrasion grooves formation (abrasive wear). The high hardness of carbides and oxides compared to steel and the angular geometry of the debris could promote the formation of abrasion striae.

The wear rate K_v was calculated with the following formula $K_v = \frac{V}{d.F_N}$ (Ref 37), where it is assumed that the volume loss V is proportional to the normal load F_N and the slip distance d. Figure 11 shows the average wear rate calculated for each sample from the three applied loads.

316L reference wear rate is 50 to 100 times higher than those of the carburized samples. This observation is in agreement with the measured hardnesses (Fig. 4): 316L shows a hardness of 180 HV_5, while the carburized samples show values higher than 500 HV_5. For the carburized sample without melting (internal carburizing), the wear rate is two times higher than the partially melted areas. This difference may be related to a lower hardness. The wear rates of the partially melted areas are equivalent. Generally, the wear volume or wear track depth increases proportionally to the applied load. 316L wear track depth increases with the applied load (Fig. 10a) in contrast to the other three zones (Fig. 10b, c, and d). The internal carburizing zone (Fig. 10d) and the Cr-depleted melting zone (Fig. 10b) show a low track depth, which remains equivalent between 1 and 5 N. For a load of 10 N, the track depth is more consistent with the systematic presence of a bump at the edge of the track, illustrating plastic deformation similar to 316L. This behavior seems to indicate the presence of a critical load at which the wear behavior changes. The increase in normal load leads to an increase in temperature. The surface oxidation is significant, the spalling of the oxide layer provides debris that gets stuck in the track, promoting the abrasion grooves formation (Fig. 10d). Figure 10c shows no change in track depth regardless of the applied load. The load or the number of cycles is not sufficient to cause the oxide layer scaling. This is explained by the high carbide proportion on the surface and the high hardness (850 HV_5).

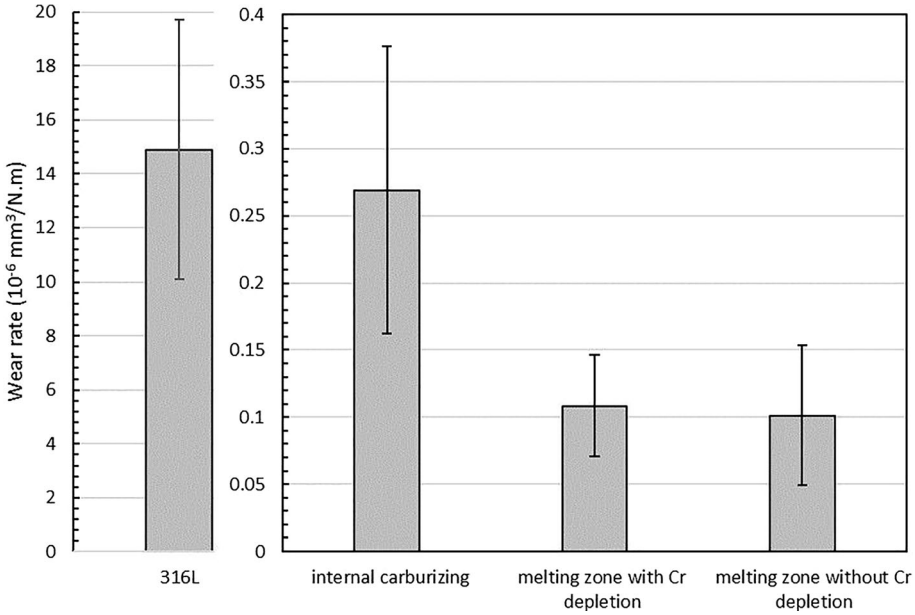

Fig. 11 Average wear rates of the different zones of interest of the sample carburized by SPS at 1100 °C under 70 MPa for 30 min

4. Conclusions

This work focused on case-hardening of austenitic 316L stainless steel using the SPS process (1100 °C; 70 MPa) near the solid/liquid state temperature. The kinetic growth of the internal carburizing layer follows a parabolic law with $k_p^{(i)} \approx 10^{-7}$ cm^2/s, while the melting front follows a linear law with $k_l = 1.0 \times 10^{-4}$ cm^2/s.

The case-hardened layer is composed by three distinct zones: internal carburizing, carburizing with melting, and carburizing with melting and depletion of Cr. All these zones are composed of mixed carbides $(Cr_{0.4}Fe_{0.6})_7C_3$ distributed in an austenitic matrix. The internal solid-state carburizing allows reaching carbide diameters of 3 μm, with an amount of approximately 40%, and for 500 HV_5. The wear mechanism is mainly abrasive with the generation of debris (oxide, carbide) trapped in the wear track, favoring abrasion grooves formation, as for 316L behavior. Partial melting favors the formation of a dense carbide layer with carbide diameters from 5 to 10 times larger than those of the internal carburizing zone. The surface amount of carbides, having a hardness of 850 HV_5, reaches 60%. Oxidative wear seems to predominate with consequent oxide plate formation in the wear track. The wear rate achieved in the partial melting zone is two times lower than in the areas with internal carburizing. For long holding times, a chromium depletion zone with Mo-rich intermetallic phases appears in the melting zone, between the surface and this dense carbide layer. The wear test shows spalling of the oxide layer in contrast to the melting zone without Cr depletion, where the oxide layer remains well-adherent.

References

1. A.J. Mackie, G.D. Hatton, H.G.C. Hamilton, J.S. Dean, and R. Goodall, Carbon Uptake and Distribution in Spark Plasma Sintering (SPS) Processed Sm (Co, Fe, Cu, Zr)$_z$, *Mater. Lett.*, 2016, **171**, p 14–17. https://doi.org/10.1016/j.matlet.2016.02.049
2. G. Bernard-Granger, N. Benameur, C. Guizard, and M. Nygren, Influence of Graphite Contamination on the Optical Properties of Transparent Spinel Obtained by Spark Plasma Sintering, *Scr. Mater.*, 2009, **60**, p 164–167. https://doi.org/10.1016/j.scriptamat.2008.09.027
3. V. Necina and W. Pabst, Reduction of Temperature Gradient and Carbon Contamination in Electric Current Assisted Sintering (ECAS/SPS) Using a "Saw-Tooth" Heating Schedule 2019, *Ceram. Int.*, 2019, **45**, p 22987–22990. https://doi.org/10.1016/j.ceramint.2019.07.343
4. N. Kwak, G. Min, Y. Oh, D.-W. Suh, H.C. Kim, S.-G. Kang, and H.N. Han, Tantalum and Molybdenum Barriers to Prevent Carbon Diffusion in Spark Plasma Sintered Tungsten, *Scr. Mater.*, 2021, **196**, p 113759. https://doi.org/10.1016/j.scriptamat.2021.113759
5. M.-R. Ardigo-Besnard, A. Besnard, M. Moser, and F. Bussière, Development of Ti PVD Films to Limit the Carburization of Metal Powders during SPS Process, *Solids*, 2021, **2**, p 395–406. https://doi.org/10.3390/solids2040025
6. A. Nishimoto and C. Nishi, Carbide Layer Coating on Titanium by Spark Plasma Sintering Technique, *Surf. Coat. Technol.*, 2018, **353**, p 324–328. https://doi.org/10.1016/j.surfcoat.2018.08.092
7. Y. Jiang, J.F. Yang, R. Liu, X.P. Wang, and Q.F. Fang, Oxidation and Corrosion Resistance of WC Coated Tungsten Fabricated by SPS Carburization, *J. Nucl. Mater.*, 2014, **450**, p 75–80. https://doi.org/10.1016/j.jnucmat.2013.05.050
8. H. Yanjun, L. Jinxu, L. Jianchong, L. Shukui, Z. Qinghe, and C. Xingwang, Rapide Preparation of TiC Reinforced Ti_6Al_4V Based Composites by Carburizing Method through Spark Plasma Sintering Technique, *Mater. Des.*, 2015, **65**, p 94–97. https://doi.org/10.1016/j.matdes.2014.09.008
9. M. Omori, Sintering, Consolidation, Reaction and Crystal Growth by the Spark Plasma System (SPS), *Mater. Sci. Eng. A*, 2000, **287**, p 183–188. https://doi.org/10.1016/S0921-5093(00)00773-5
10. M.Z. Becker, N. Shomrat, and Y. Tsur, Recent Advances in Mechanism Research and Methods for Electric-Field-Assisted Sintering of Ceramics, *Adv. Mater.*, 2018, **30**, p 1706369. https://doi.org/10.1002/adma.201706369
11. R. Ranjan and A. Kumar Das, Protection from Corrosion and Wear by Different Weld Cladding Techniques: A Review, *Mater. Today Proc.*, 2022, **57**, p 1687–1693. https://doi.org/10.1016/j.matpr.2021.12.329
12. A.I. Gorunov, Investigation of M_7C_3, $M_{23}C_6$ and M_3C Carbides Synthesized on Austenitic Stainless Steel and Carbon Fibers Using Laser Metal Deposition, *Surf. Coat. Technol.*, 2020, **401**, p 126294. https://doi.org/10.1016/j.surfcoat.2020.126294
13. U. Anselmi-Tamburini, S. Gennari, J.E. Garay, and Z.A. Munir, Fundamental Investigations on the Spark Plasma Sintering/Synthesis Process II. Modeling of Current and Temperature Distributions, *Mater. Sci. Eng. A*, 2005, **394**, p 139–148. https://doi.org/10.1016/j.msea.2004.11.019
14. Y. Aman, V. Granier, and E. Djurado, Pressure-Less Spark Plasma Sintering Effect on Non-conventional Necking Process during the Initial Stage of Sintering of Copper and Alumina, *J. Mater. Sci.*, 2012, **47**, p 5766–5773. https://doi.org/10.1007/s10853-012-6469-0
15. Z.A. Munir, U. Anselmi-Tamburini, and M. Ohyanagi, The Effect of Electric Field and Pressure on the Synthesis and Consolidation of Materials: A Review of the Spark Plasma Sintering Method, *J. Mater. Sci.*, 2006, **41**, p 763–777. https://doi.org/10.1007/s10853-006-6555-2
16. H. Sabet, S. Mirdamadi, S. Kheirandish, and M. Goodarzi, SEM and XRD Study of Hypoeutectic Fe-Cr-C Hardfacing Alloy Microstructure in as Weld Condition, *J. Appl. Chem. Res.*, 2010, **78**, p 70–78.
17. X.-M. He, X.-B. Liu, M.-D. Wang, M.-S. Yang, S.-H. Shi, G.-Y. Fu, and S.-F. Chen, Elevated Temperature Dry Sliding Wear Behavior of Nickel-Based Composited Coating on Austenitic Stainless Steel Deposited by a Novel Central Hollow Laser Cladding, *Appl. Surf. Sci.*, 2011, **258**, p 535–541. https://doi.org/10.1016/j.apsusc.2011.08.072
18. S. Buytoz, Microstructure Properties of M_7C_3 Eutectic Carbides in a Fe-Cr-C Alloy, *Mater. Lett.*, 2006, **60**, p 605–608. https://doi.org/10.1016/j.matlet.2005.09.046
19. S. Ma, J. Xing, Y. He, Y. Li, Z. Huang, G. Liu, and Q. Geng, Microstructure and Crystallography of M_7C_3 Carbide in Chromium Cast Iron, *Mater. Chem. Phys.*, 2015, **161**, p 65–73. https://doi.org/10.1016/j.matchemphys.2015.05.008
20. A.F. Padilha and P.R. Rios, Decomposition of Austenite in Austenitic Stainless Steels, *ISIJ Int.*, 2002, **42**, p 325–337. https://doi.org/10.2355/isijinternational.42.325
21. Y.L. Su, T.H. Liu, C.T. Su, J.P. Yur, W.H. Kao, and S.H. Yao, Tribological Characteristics and Cutting Performance of $Cr_{x\%}C$-Coated Carbide Tools, *J. Mater. Process. Technol.*, 2004, **153–154**, p 699–706. https://doi.org/10.1016/j.jmatprotec.2004.04.093
22. S.C. Kwon, M. Kim, S.U. Park, D.Y. Kim, D. Kim, K.S. Nam, and Y. Choi, Characterization of Intermediate Cr-C Layer Fabricated by Electrodeposition in Hexavalent and Trivalent Chromium Baths, *Surf. Coat. Technol.*, 2003, **183**, p 151–156. https://doi.org/10.1016/j.surfcoat.2003.09.069
23. T. Murakami, K. Kaneda, M. Nakano, H. Mano, A. Korenaga, and S. Sasaki, Friction and Wear Properties of Fe-Mo Intermetallic Compounds under Oil Lubrication, *Intermetallics*, 2007, **15**, p 1573–1581. https://doi.org/10.1016/j.intermet.2007.06.008
24. S.Y. Kondrat'ev, V.S. Kraposhin, G.P. Anastasiadi, and A.L. Talis, Experimental Observation and Crystallographic Description of M_7C_3 Carbide Transformation in Fe-Cr-Ni-C HP Type Alloy, *Acta Mater.*, 2015, **100**, p 275–281. https://doi.org/10.1016/j.actamat.2015.08.056
25. K. Wieczerzak, P. Bala, R. Dziurka, T. Tokarski, G. Cios, T. Koziel, and L. Gondek, The Effect of Temperature on the Evolution of Eutectic Carbides and $M_7C_3M_{23}C_6$ Carbides Reaction in the Rapidly Solidified Fe-Cr-C Alloy, *J. Alloys Compd.*, 2017, **698**, p 673–684. https://doi.org/10.1016/j.jallcom.2016.12.252
26. A. Inoue and T. Masumoto, Carbide Reactions (M3C → M7C3 → M23C6 → M6C) during Tempering of Rapidly Solidified High Carbon Cr-W and Cr-Mo Steels, *Metall. Trans. A*, 1980, **11**, p 739–747. https://doi.org/10.1007/BF02661203

27. D.J. Young, *High Temperature Oxidation and Corrosion of Metals, Chapter 9: Corrosion by Carbon*, 2nd ed. Elsevier Science, Amsterdam, 2016, p 431–493
28. J. Crank, *The Mathematics of Diffusion*, 2nd ed. Clarendon Press, Oxford, 1975
29. F. Ernst, Y. Cao, G.M. Michal, and A.H. Heuer, Carbide Precipitation in Austenitic Stainless Steel Carburized at Low Temperature, *Acta Mater.*, 2007, **55**, p 1895–1906. https://doi.org/10.1016/j.actamat.2006.09.049
30. R.P. Agarwala, M.C. Naik, M.S. Anand, and A.R. Paul, Diffusion of Carbon in Stainless Steels, *J. Nucl. Mater.*, 1970, **36**, p 41–47. https://doi.org/10.1016/0022-3115(70)90060-7
31. J. Cermak and L. Kral, Carbon Diffusion in Carbon-Supersaturated Ferrite and Austenite, *J. Alloys Compd.*, 2014, **586**, p 129–135. https://doi.org/10.1016/j.jallcom.2013.10.058
32. Y. Sarikaya, M. Önal, and A.D. Pekdemir, Application of Diffusion and Transition State Theories on the Carburizing of Steel AISI 316 by Annealing in Uranium Carbide Powder, *Heliyon*, 2019, **5**, p e02305. https://doi.org/10.1016/j.heliyon.2019.e02305
33. C. Yang, D.G. Mo, H.Z. Lu, X.Q. Li, W.W. Zhang, Z.Q. Fu, L.C. Zhang, and E.J. Lavernia, Reaction Diffusion Rate Coefficient Derivation by Isothermal Heat Treatment in Spark Plasma Sintering System, *Scr. Mater.*, 2017, **134**, p 91–94. https://doi.org/10.1016/j.scriptamat.2017.03.005
34. U. Anselmi-Tamburini, J.E. Garay, and Z.A. Munir, Fundamental Investigations on the Spark Plasma Sintering/Synthesis Process: III. Current Effect on Reactivity, *Mater. Sci. Eng. A*, 2005, **407**, p 24–30. https://doi.org/10.1016/j.msea.2005.06.066
35. M.C.S. Duarte, C. Godoy, and J.C. Avelar-Batista Wilson, Analysis of Sliding Wear Tests of Plasma Processed AISI 316L Steel, *Surf. Coat. Technol.*, 2014, **260**, p 316–325. https://doi.org/10.1016/j.surfcoat.2014.07.094
36. F. Rotundo, L. Ceschini, C. Martini, R. Montanari, and A. Varone, High Temperature Tribological Behavior and Microstructural Modifications of the Low-Temperature Carburized AISI 316L Austenitic Stainless Steel, *Surf. Coat. Technol.*, 2014, **258**, p 772–781. https://doi.org/10.1016/j.surfcoat.2014.07.081
37. J.F. Archard, Contact and Rubbing of Flat Surface, *J. Appl. Phys.*, 1953, **24**, p 981–988. https://doi.org/10.1063/1.1721448